Direct ink writing of 3D thermoelectric architectures for fabrication of micro power generators

Fredrick Kim[1†], Seong Eun Yang[1†], Hyejin Ju[1†], Seungjun Choo[1], Jungsoo Lee[1], Gyeonghun Kim[2], Soo-ho Jung[3], Suntae Kim[1], Chaenyung Cha[1], Kyung Tae Kim[3], Sangjoon Ahn[2], Han Gi Chae[1*], and Jae Sung Son[1,4*]

[1]*Department of Materials Science and Engineering, Ulsan National Institute of Science and Technology (UNIST), Ulsan 44919, Republic of Korea*

[2]*Department of Nuclear Engineering, Ulsan National Institute of Science and Technology (UNIST), Ulsan 44919, Republic of Korea*

[3]*Department for 3D Printing Materials, Korea Institute of Materials Science (KIMS), 797 Changwon-daero, Gyeongnam 51508, Republic of Korea*

[4]*Center for Future Semiconductor Technology (FUST), Ulsan National Institute of Science and Technology (UNIST), Ulsan 44919, Republic of Korea*

[†]*These authors contributed equally to this work.*

*e-mail: hgchae@unist.ac.kr (H.G.C.) and jsson@unist.ac.kr (J.S.S.)

This supplement contains

Supplementary Figures 1-15

Supplementary Discussion

Supplementary References

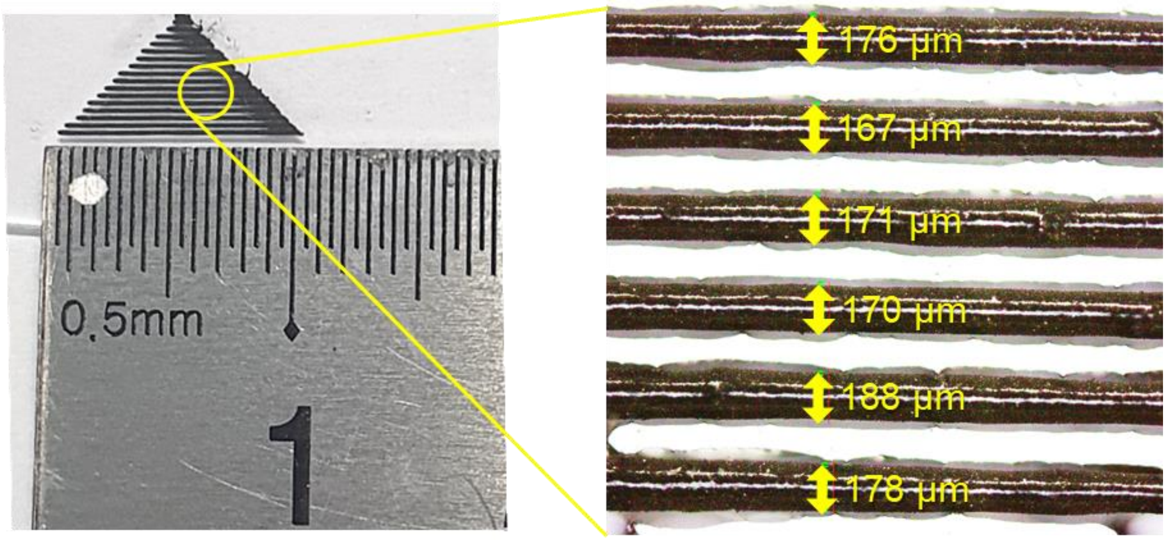

Supplementary Fig. 1 | Line uniformity test. Photograph and OM image of the laterally printed layers.

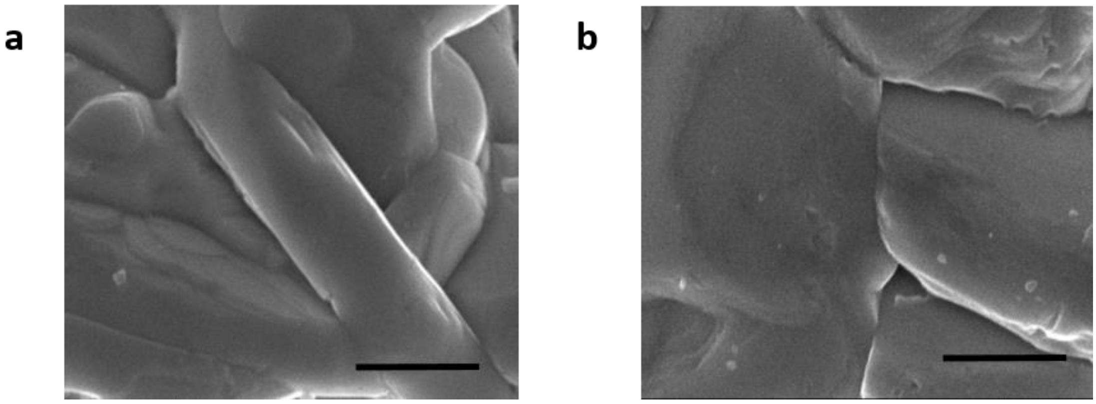

Supplementary Fig. 2 | Microstructural analysis of the 3D-written filaments. a,**b**, High-magnification SEM image of the (a) n-type and (b) p-type filaments. Scale bar, 1 μm.

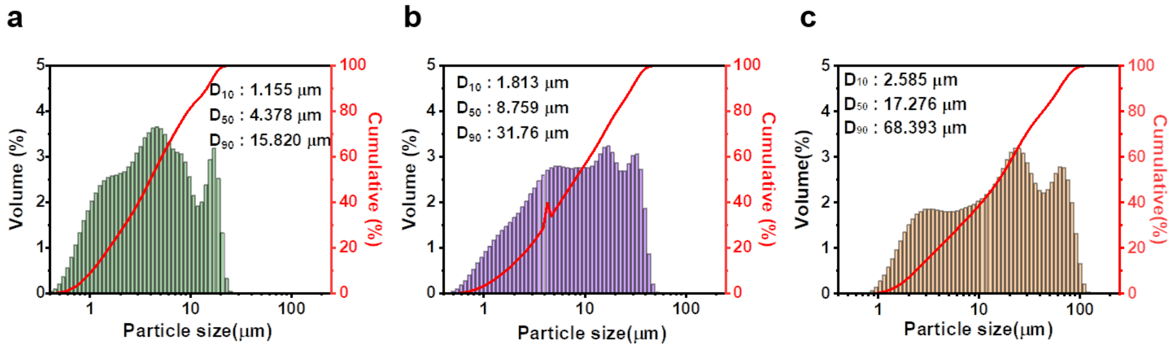

Supplementary Fig. 3 | Particle size distribution. a–c, Particle size histograms of the $Bi_{0.55}Sb_{1.45}Te_3$ TE particles synthesized by the ball-milling process under the different synthetic conditions. D_{10}, D_{50}, D_{90} denote the particle diameter at the cumulative percentages of 10, 50, and 90%.

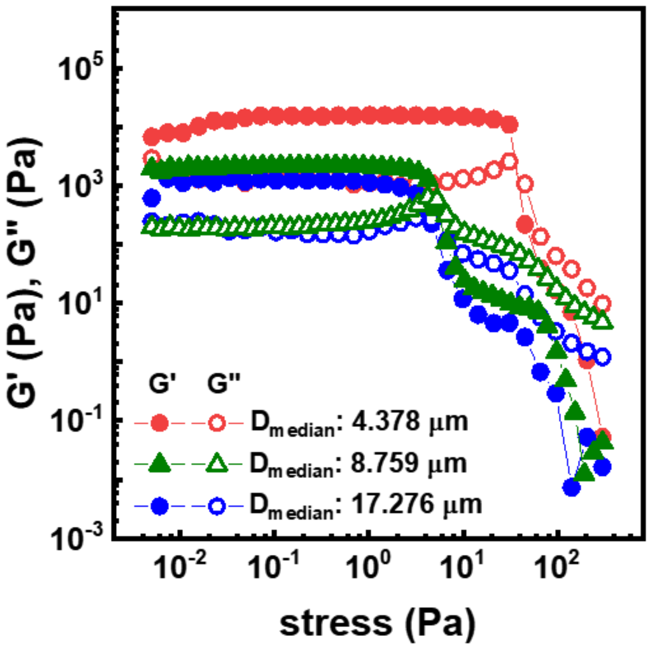

Supplementary Fig. 4 | The storage(G') and loss(G") moduli of $Bi_{0.55}Sb_{1.45}Te_3$ TE particle inks from stress sweep test by particle size.

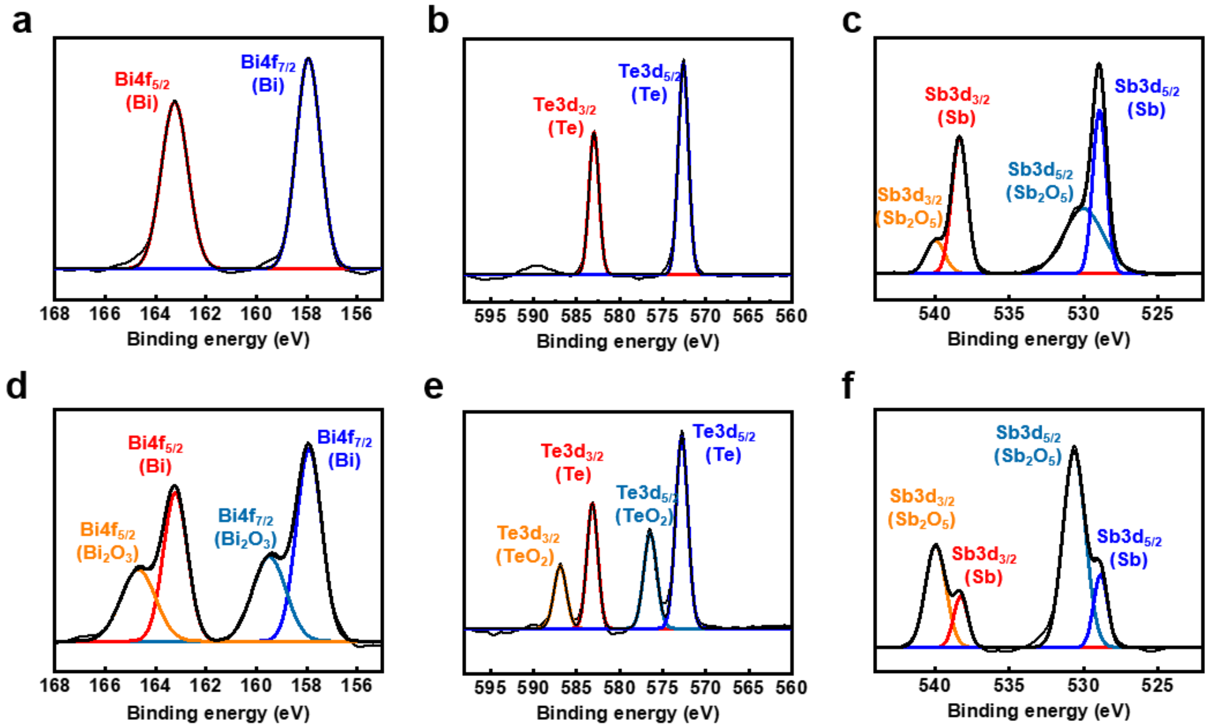

Supplementary Fig. 5 | XPS analysis of $Bi_{0.55}Sb_{1.45}Te_3$ TE particles. a–c, Experimental and fitted XPS spectra of the non-oxidised $Bi_{0.55}Sb_{1.45}Te_3$ particles in the regions of Bi4f (**a**), Te3d (**b**), and Sb3d (**c**). **d–f**, Experimental and fitted XPS spectra of the oxidised $Bi_{0.55}Sb_{1.45}Te_3$ particles in the regions of Bi4f (**d**), Te3d (**e**), and Sb3d (**f**). The XPS spectrum of non-oxidised particles in the panels (a)-(c) shows negligible or tiny peaks corresponding to those of oxides phase, while the peaks related to oxidation such as the Bi_2O_3, TeO_2, and Sb_2O_5 phases were clearly observed in XPS spectrum of the oxidised particles (panels (d)-(f)).

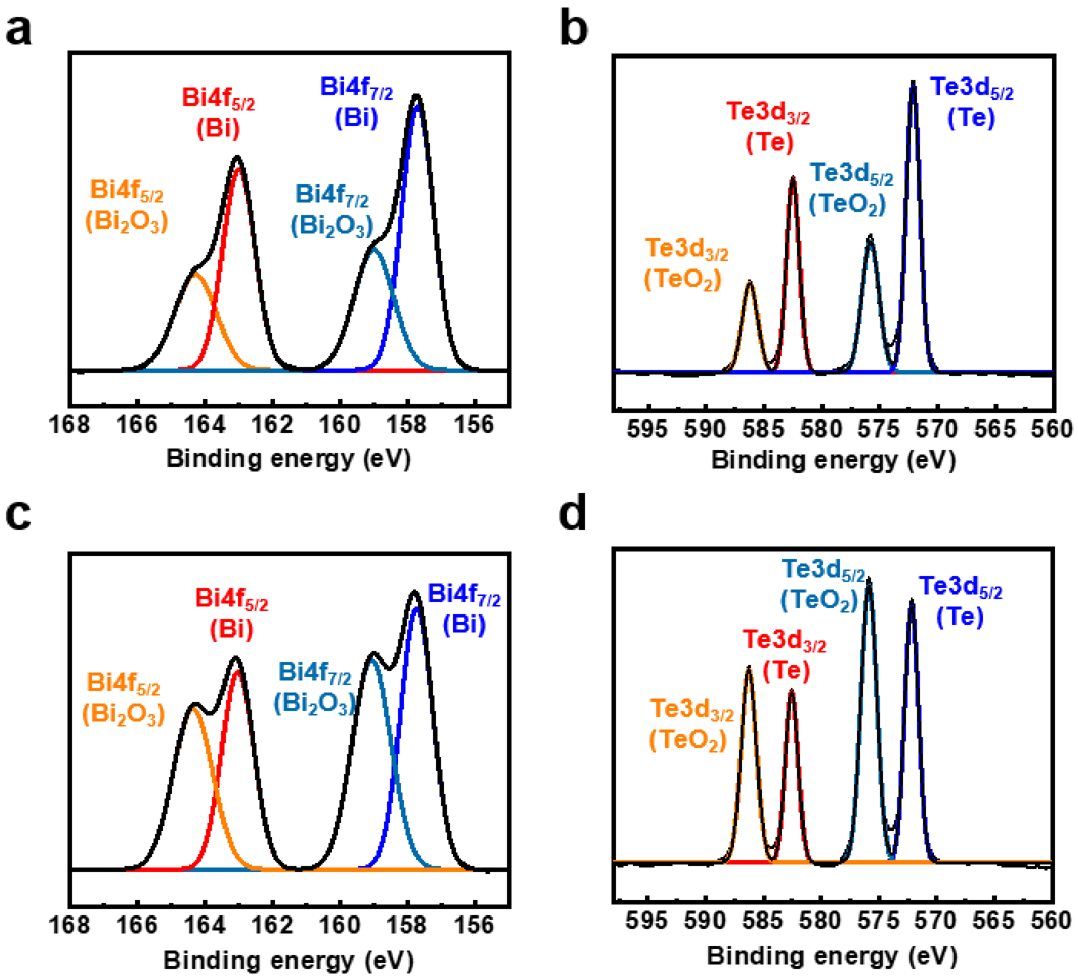

Supplementary Fig. 6 | X-ray Photoelectron Spectroscopy (XPS) analysis of $Bi_2Te_{2.7}Se_{0.3}$ TE particles. a,**b**, Experimental and fitted XPS spectra of the non-oxidised $Bi_2Te_{2.7}Se_{0.3}$ in the regions of Bi 4f (**a**), and Te 3d (**b**). **c**,**d**, Experimental and fitted XPS spectra of the oxidised $Bi_2Te_{2.7}Se_{0.3}$ particles in the regions of showing Bi 4f (**c**), and Te 3d (**d**). The XPS spectrum of non-oxidised particles in the panels (a)-(c) shows small peaks corresponding to those of the oxides phase, not agreeing with the XPS spectrum of p-type $Bi_{0.55}Sb_{1.45}Te_3$, in which the oxidation peaks were observed in the only Sb 3d region. This can be attributed to the oxygen affinity differences in Bi, Sb, and Te, where that for Sb is much higher than those for other elements[S1]. Thus, Sb was preferentially oxidised in p-type $Bi_{0.55}Sb_{1.45}Te_3$ particles but both Bi and Te were simultaneously oxidised in n-type $Bi_2Te_{2.7}Se_{0.3}$ particles. After the oxidation, the peaks related to oxidation such as the Bi_2O_3 and TeO_2 phases were significantly pronounced, indicating the further surface oxidation of particles.

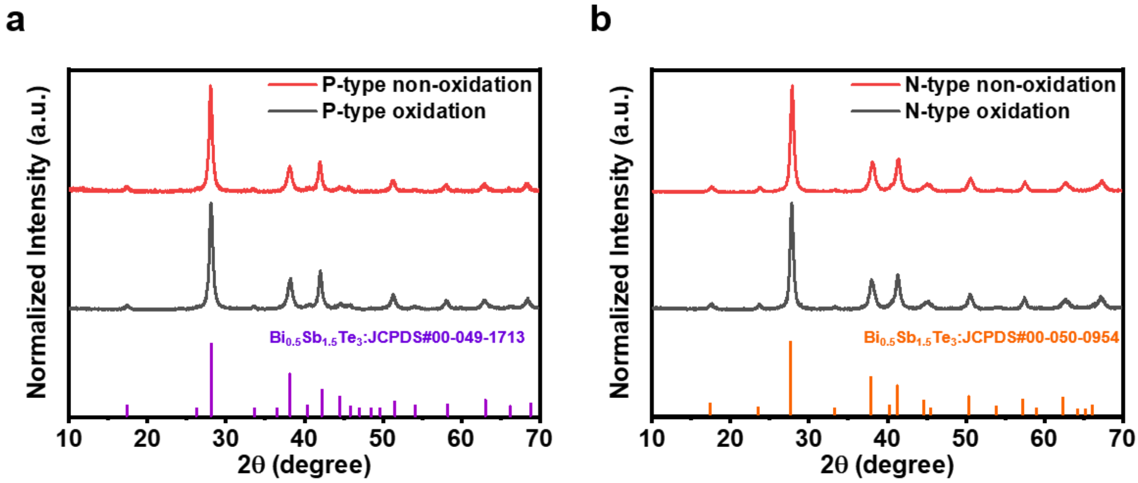

Supplementary Fig. 7 | XRD patterns of mechanically alloyed (Bi, Sb)$_2$(Te, Se)$_3$-based particles. **a–c**, XRD patterns of the 3D-printed $Bi_{0.55}Sb_{1.45}Te_3$ (**a**) and $Bi_2Te_{2.7}Se_{0.3}$ (**b**) filaments before and after the oxidation. The vertical lines indicate peaks corresponding to bulk $Bi_{0.5}Sb_{1.5}Te_3$ (Joint Committee on Powder Diffraction Standards, JCPDS: 00-049-1713) and $Bi_2Te_{2.7}Se_{0.3}$ (JCPDS: 00-015-0863)

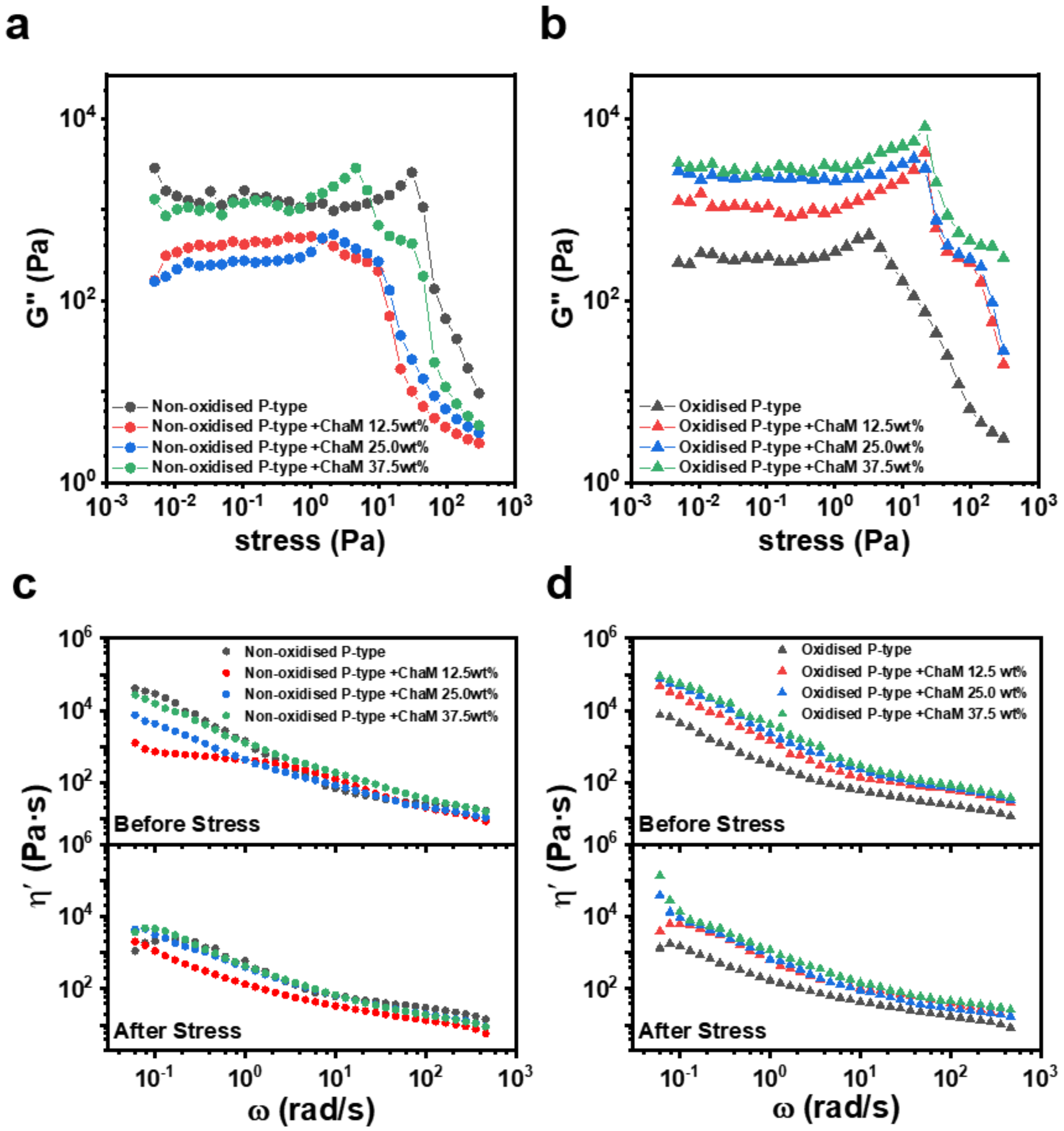

Supplementary Fig. 8 | Various viscoelastic properties of $Bi_{0.55}Sb_{1.45}Te_3$ TE particle inks at various ChaM contents. a–d, The loss modulus (G") of (**a**) non-oxidised and (**b**) oxidised particle inks from the stress sweep test, and the dynamic viscosity (η') curves of (**c**) non-oxidised and (**d**) oxidised particle inks from the frequency sweep test before and after 300 Pa of shear stress.

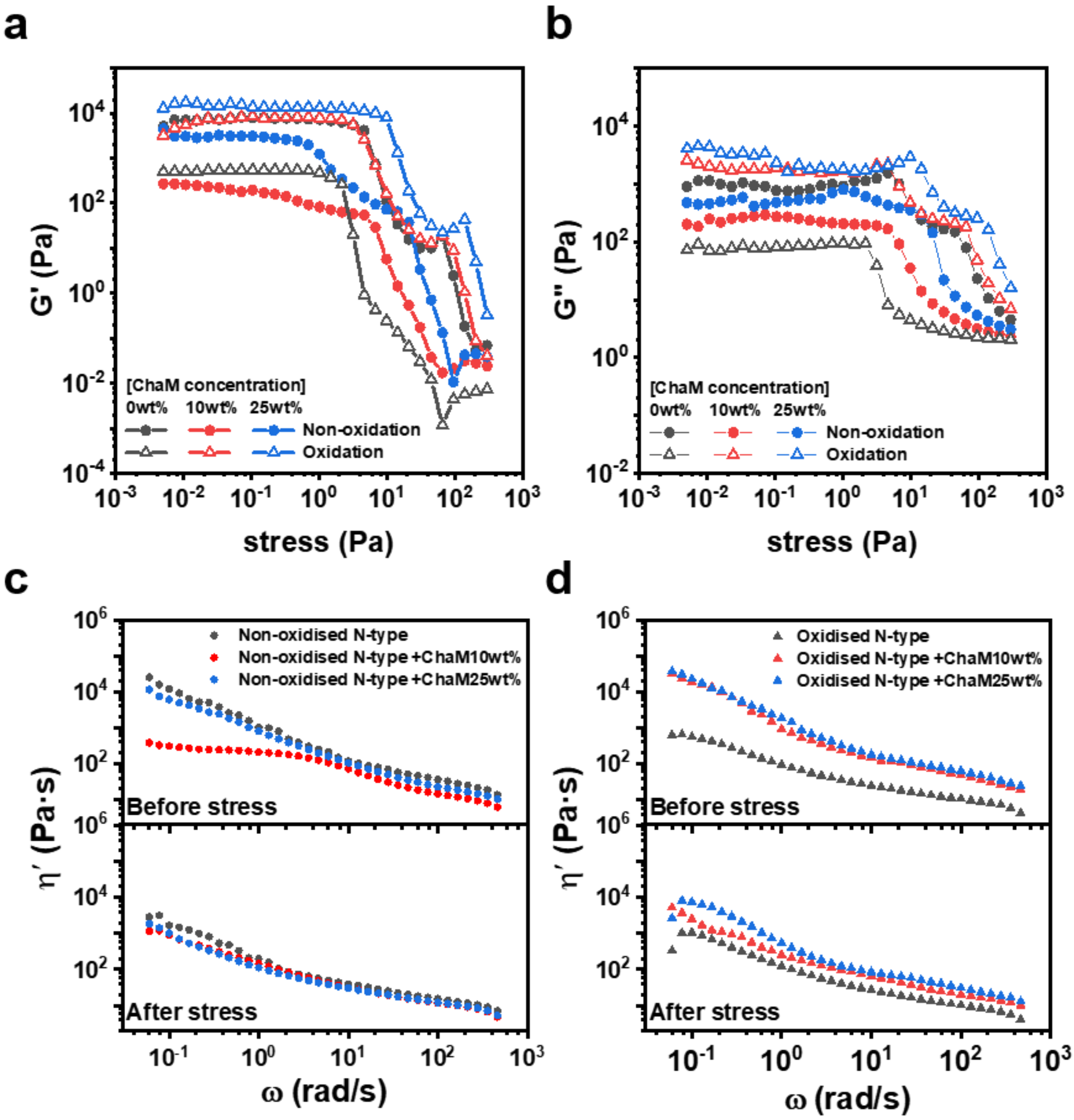

Supplementary Fig. 9 | Various viscoelastic properties of $Bi_2Te_{2.7}Se_{0.3}$ TE particle inks at various ChaM contents. a–d, The loss modulus (G”) of (**a**) non-oxidised and (**b**) oxidised inks from the stress sweep test, and the dynamic viscosity (η’) curves of (**c**) non-oxidised and (**d**) oxidised inks from the frequency sweep test before and after 300 Pa of shear stress.

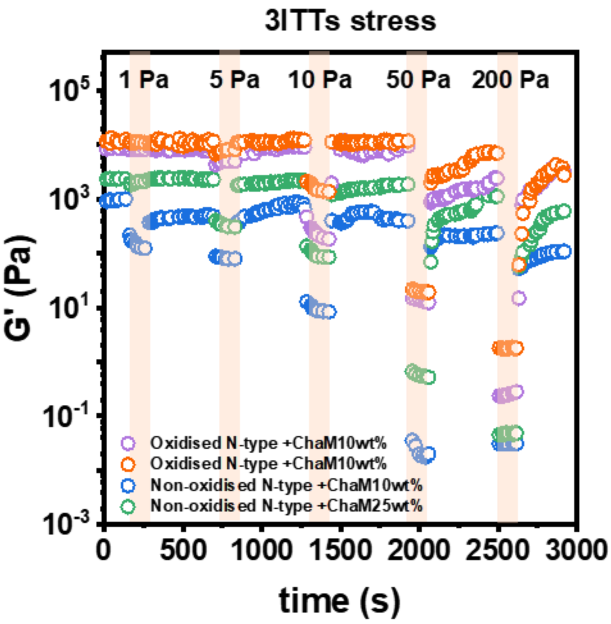

Supplementary Fig. 10 | Storage modulus (G') of $Bi_2Te_{2.7}Se_{0.3}$ TE particle inks containing various ChaM contents in the sequential 3ITTs measurement.

.

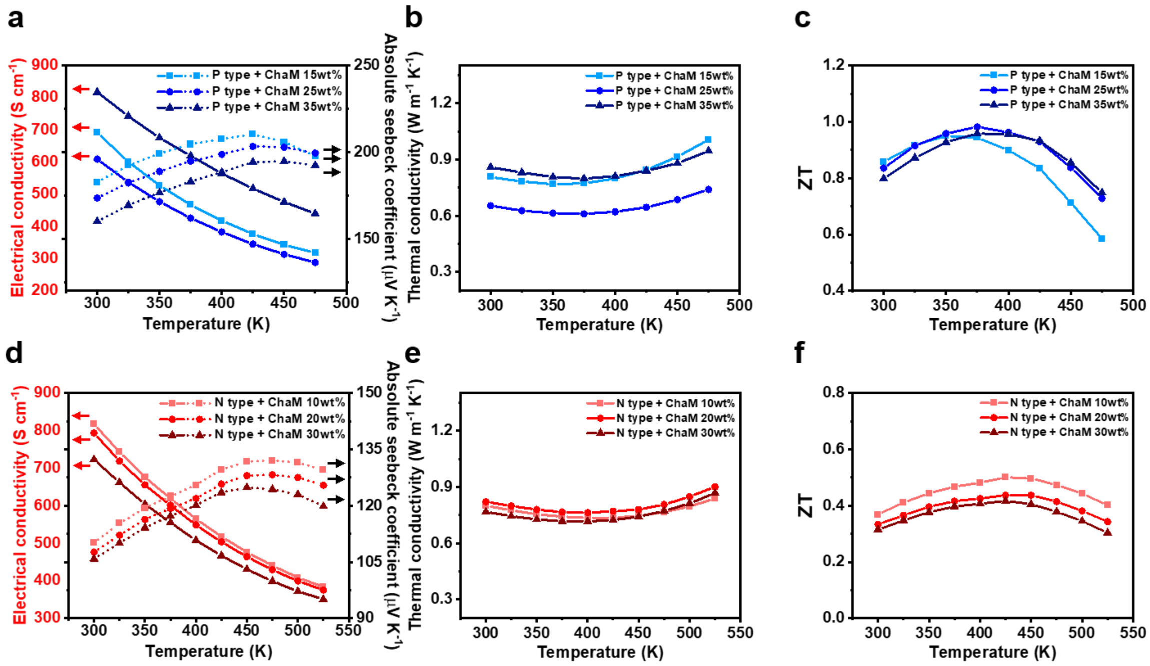

Supplementary Fig. 11 | TE properties of the 3D-printed TE bulk cuboids with different ChaM contents. a–c, Temperature-dependent TE properties of the p-type $Bi_{0.55}Sb_{1.45}Te_3$ 3D-printed cuboids with different ChaM contents: electrical conductivity and absolute Seebeck coefficient (**a**), thermal conductivity (**b**) and *ZT* (**c**). **d–f**, Temperature-dependent TE properties of the n-type $Bi_2Te_{2.7}Se_{0.3}$ 3D-printed cuboids with different ChaM contents: electrical conductivity and absolute Seebeck coefficient (**d**), thermal conductivity (**e**) and *ZT* (**f**).

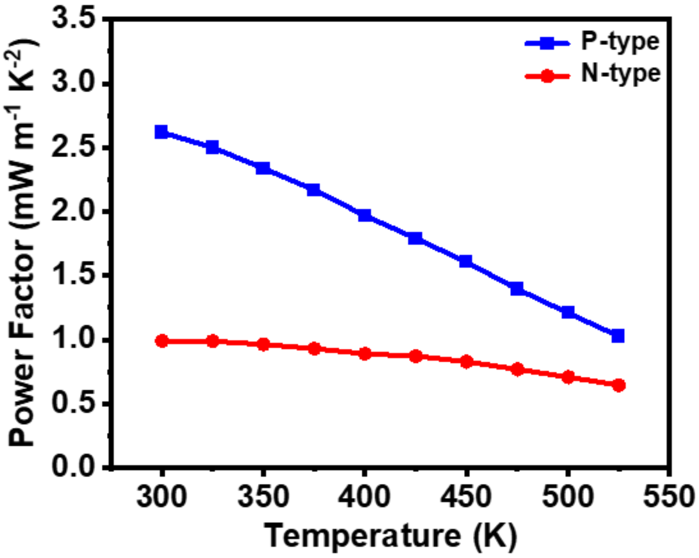

Supplementary Fig. 12 | The TE power factors of the 3D-printed samples.

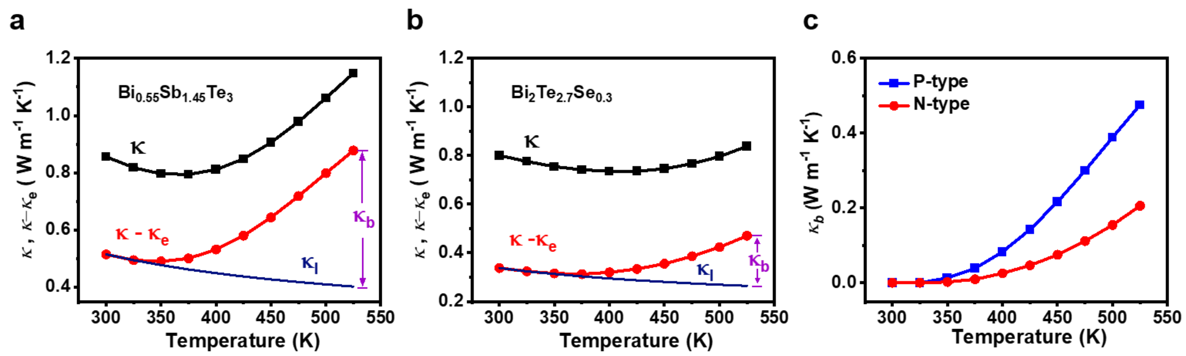

Supplementary Fig. 13 | Temperature-dependent lattice & bipolar thermal conductivities. a–c, Calculated lattice & bipolar thermal conductivities of the p-type (**a**) and n-type (**b**) 3D-printed TE bulk cuboids and comparison for the bipolar thermal conductivities of the n-type and p-type (**c**).

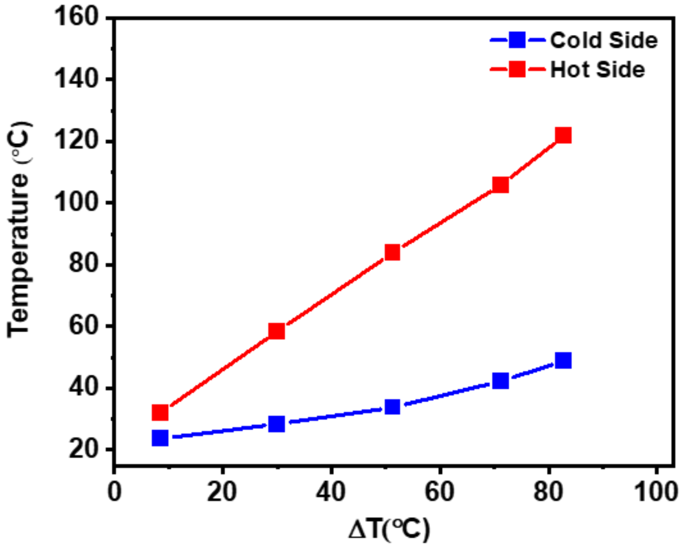

Supplementary Fig. 14 | Temperatures of the hot and cold sides of the μ-TEG in the measurement set-up under heating.

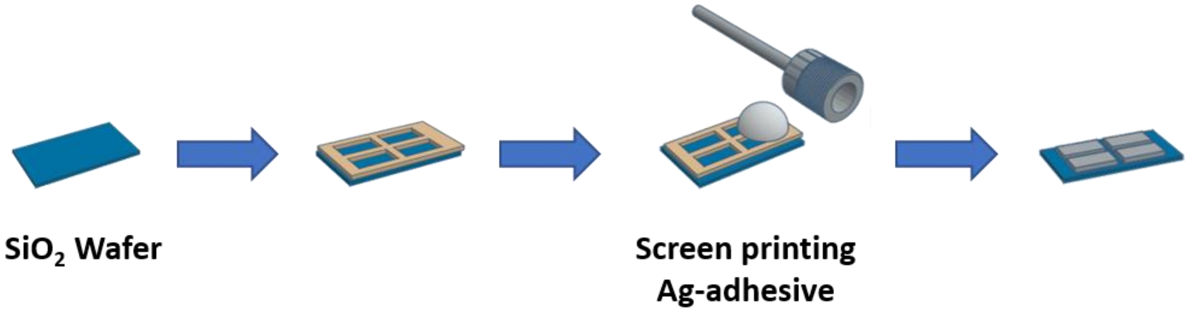

Supplementary Fig. 15 | Schematic illustration of the screen-printing of patterned Ag electrodes.

Supplementary Discussion

Calculation of the lattice & bipolar thermal conductivities

The p-type sample exhibited a positive temperature dependence of thermal conductivity, whereas the n-type sample exhibited an almost constant value. To understand the temperature dependence, we calculated the lattice and bipolar thermal conductivities according to the relationship $\kappa = \kappa_e + \kappa_l + \kappa_{bi}$. Based on the Wiedemann–Franz law, κ_e was estimated as $\kappa_e = L\sigma T$, where T is the absolute temperature, σ is the electrical conductivity, and L is the Lorenz number. For each sample, L was calculated from the experimentally determined Seebeck coefficient using the single parabolic model proposed by Kim et al.[S2]: $L = 1.5 + (\exp \frac{|S|}{116})$.

After the electronic contribution κ_e was subtracted, κ decreased with the temperature in the low-temperature range and stabilised or increased at higher temperatures, where the bipolar contribution, κ_{bi}, became significant (Supplementary Fig. 13).

Above the Debye temperature (θ_D), which is 165 K for Bi_2Te_3 and approximately 160 K for $Bi_{0.5}Sb_{1.5}Te_3$[S3,S4], phonon scattering by the Umklapp mechanism leads to the T^{-1} dependence of the lattice thermal conductivity, κ_l. On the other hand, κ_{bi} exhibits an exponential dependence on the temperature and material bandgap, E_g[S5] :

$$\kappa_{bi} \propto \exp\left(-\frac{E_g}{2k_BT}\right)$$

To estimate κ_{bi}, we linearly fitted (κ - κ_e) vs. T^{-1} in the low-temperature range and extrapolated the data to higher temperatures (Supplementary Fig. 13). The band gap of the n-type sample (E_g = 0.126 eV) was larger than that of the p-type sample (E_g = 0.184 eV). The band gap can be estimated from the value of S_{max} at T_{max}:

$$E_g = 2eS_{max}T_{max}$$

The band gap of the n-type sample was relatively wide (0.184 eV), leading to the suppression of the bipolar effect, whereas that of the p-type sample was relatively narrow (0.126 eV), which was responsible for the increase in the bipolar contribution at elevated temperatures. The temperature dependence of thermal conductivities was caused by the different bipolar contributions.

Supplementary References

S1. Volykhov AA. et al. Can surface reactivity of mixed crystals be predicted from their counterparts? A case study of $(Bi_{1-x}Sb_x)_2Te_3$ topological insulators. *J. Mater. Chem. C* **6**, 8941-8949 (2018).

S2. Kim, S. I. et al. Thermoelectrics. Dense dislocation arrays embedded in grain boundaries for high-performance bulk thermoelectrics. *Science* **348**, 109-114 (2015).

S3. Blank, V. D. et al. Thermoelectric properties of $Bi_{0.5}Sb_{1.5}Te_3/C_{60}$ nanocomposites. *Phys. Rev. B.* **86**, (2012).

S4. Rowe, D. M. CRC Handbook of Thermoelectrics. **1**, (1995).

S5. Bahk, J.-H. & Shakouri, A. Minority carrier blocking to enhance the thermoelectric figure of merit in narrow-band-gap semiconductors. *Phys. Rev. B.* **93**, (2016).